

Learning Robust Control Policies for Inverted Pose on Miniature Blimp Robots

Yuanlin Yang, Lin Hong, and Fumin Zhang[†]

Abstract—The ability to achieve and maintain inverted poses is essential for unlocking the full agility of miniature blimp robots (MBRs). However, developing reliable control methods for MBRs remains challenging due to their complex and underactuated dynamics. To address this challenge, we propose a novel framework that enables robust control policy learning for inverted pose on MBRs. The proposed framework operates through three core stages: First, a high-fidelity three-dimensional (3D) simulation environment was constructed, which was calibrated against real-world MBR motion data to ensure accurate replication of inverted-state dynamics. Second, a robust policy for MBR inverted control was trained within the simulation environment via a domain randomization strategy and a modified Twin Delayed Deep Deterministic Policy Gradient (TD3) algorithm. Third, a mapping layer was designed to bridge the sim-to-real gap for the learned policy deployment. Comprehensive evaluations in the simulation environment demonstrate that the learned policy achieves a higher success rate compared to the energy-shaping controller. Furthermore, experimental results confirm that the learned policy with a mapping layer enables an MBR to achieve and maintain a fully upside-down pose in real-world settings.

I. INTRODUCTION

The potential of agile flying in Unmanned Aerial Vehicles (UAVs) has been extensively demonstrated through proportional integration differentiation (PID) control [1], model predictive control (MPC) [2], and deep reinforcement learning (DRL) [3], [4]. However, for MBRs, a distinct category of aerial platforms, a significant gap remains in the development of advanced control strategies capable of delivering comparable agility. UAVs typically rely on high-speed rotating propellers for lift and maneuvering, thus face inherent limitations such as high energy consumption and safety risks in proximity to humans. Unlike UAVs, MBRs leverage buoyant gas to offset their own weight, complemented by low-power thrusters for fine-grained motion adjustment. This unique design has positioned MBRs as a promising solution for various applications, such as entertainment and advertising [5], warehouse inventory management [6], indoor environmental monitoring [7], and infrastructure inspection [8].

Existing research on MBRs has predominantly centered on innovative structural design, such as the optimization of envelope shape, gondola layout, and payload integration to enhance operational stability and adaptability [9], [10], and focused on slight pitch or yaw adjustments to maintain basic hovering [11] or low-speed navigation [12]. However, the fully agile movement control of MBRs, a capability that would enable rapid attitude transitions and wide-range position adjustments, remains a challenge. This challenge arises from the unique dynamic properties of MBRs. In low-

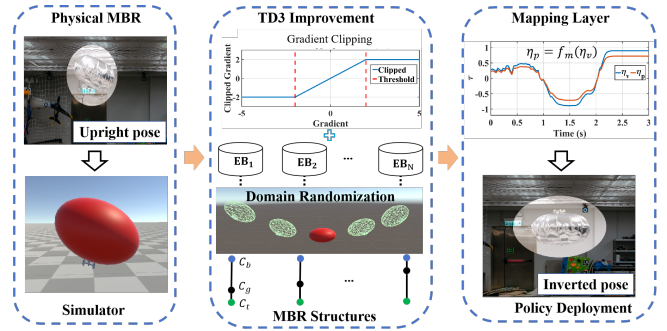


Fig. 1: Overview of the proposed method for inverted control of MBRs. The MBR with an upright pose can reach and maintain the inverted pose with the learned robust policy.

speed small UAV applications, aerodynamic drag is typically negligible relative to the total thrust since UAVs rely on high-power thrusters to counteract their full weight, and their thrust output far exceeds the drag forces encountered during low-speed motion. For MBRs, two key characteristics reverse this relationship: (1) Dominant aerodynamic drag due to their large envelope volume; (2) Weak thrust output, as the buoyant gas already balances most of their weight, MBRs do not require high thrust to offset gravity.

These distinct dynamic properties render MBR attitude control fundamentally different from that of UAVs, making UAV control solutions inapplicable to MBRs. In addition, a review of MBR designs [9], [10], [13]–[16] further highlights a structural constraint: most MBRs adopt a gondola-envelope configuration, where the gondola, housing sensors, thrusters, and controllers, is suspended below or attached to the envelope. This structure inherently exhibits both stable and unstable equilibrium points: for example, the “upright” pose (gondola hanging below the envelope) is a stable equilibrium, while the “inverted” pose (gondola above the envelope) is unstable and difficult to maintain.

Against this backdrop, the primary task in this paper is to enable MBRs to reach and maintain an inverted pose based on DRL, as illustrated in Fig. 1. To clarify our problem: we define inverted control as the ability of an MBR to achieve and stabilize a fully upside-down pose—corresponding to an unstable equilibrium state where the MBR’s center of buoyancy lies below its center of gravity. The work most closely related is a recent study by Wang and Zhang [17], which explicitly tackles the challenge of inverted control for MBRs. Their approach successfully demonstrates the achievement and maintenance of a stable inverted pose using model-based

control: an energy-shaping controller to tailor the system's energy landscape for state transitions, paired with a linear state feedback controller to suppress deviations from the target inverted state. However, the energy calculation at the core of their controller depends on time-invariant MBR dynamics, yet the model parameters are highly dynamic in real-world operations, leading to performance degradation or even loss of inverted stability under environmental disturbances. Recent progress in DRL-based control has shown promise for addressing the parameter variability and disturbance susceptibility of outdoor large-size blimp robots. Liu et al. [18] proposed a deep residual reinforcement learning method integrated with a PID controller in a closed loop. This hybrid approach improved trajectory tracking accuracy but remained limited to small-range attitude control, with no consideration of inverted states. Zou et al. [19] designed a hybrid control framework that combines robust H_∞ control with proximal policy optimization (PPO), which enhances robustness against wind disturbances and variations in buoyancy.

Despite these advances, developing DRL-based methods for inverted control of MBR remains largely unexplored. In this paper, we address this gap by presenting a robust policy specifically designed for inverted control of MBRs. Our approach combines domain randomization, multi-buffer experience replay, and a sim-to-real transfer strategy to expand the applicability of learning-based control to MBRs. By focusing on inverted control as a cornerstone of large-envelope agility, this study aims to unlock new capabilities for MBRs. The main contributions are as follows:

- To the best of our knowledge, we propose the first 3D simulation environment based on Unity [20] tailored for inverted control of MBRs. It accurately models MBR-specific dynamics and supports the generation of diverse scenarios, enabling robust policy training.
- We develop a novel framework for learning robust policies for MBR inverted control. This framework incorporates domain randomization to enhance the policy's adaptability to variations in model parameters and environmental disturbances during training, and refines the TD3 algorithm to further improve training stability.
- We design a sim-to-real transfer strategy with a mapping layer that aligns simulated and real-world MBR dynamics. Experimental results show that our learned control policy achieves a reliable inverted pose of a physical MBR without further policy training.

II. PROBLEM FORMULATION

A. Dynamic Model of MBRs

As shown in Fig. 2, the MBR consists of an envelope and a gondola: the envelope is to supply the buoyancy, while the gondola is to provide a platform for housing thrusters and other electrical devices. Based on the first principle and [12], [21], the dynamic model of the MBR can be generally expressed as:

$$(\mathbf{M}_{rb} + \mathbf{M}_a)\dot{\mathbf{v}}_{b/e}^b + (\mathbf{C}_{rb} + \mathbf{C}_a)\mathbf{v}_{b/e}^b + \mathbf{\Gamma}^d + \mathbf{\Gamma}^{gb} + \mathbf{\Gamma}^e = \mathbf{\Gamma}^t, \quad (1)$$

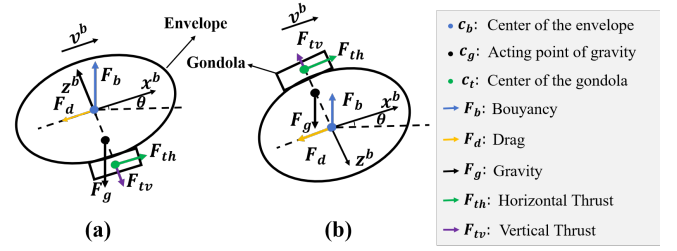


Fig. 2: Dynamic model analysis of the MBR: (a) Upright pose; (b) Inverted pose.

where $\mathbf{\Gamma}^d$ denotes air drag, $\mathbf{\Gamma}^t$ and $\mathbf{\Gamma}^e$ correspond to thruster-generated and environmental forces and torques, respectively. $\mathbf{\Gamma}^{gb}$ involves the restoring force and torque.

The dynamic models near the upright and inverted poses are shown in Figures 2 (a) and (b), respectively. In both cases, the MBR operates at a constant velocity while holding a stable attitude. Based on the force analysis, we have

$$\mathbf{F}_{th}r_t^b + m_{rb}\mathbf{g}r_z^b \sin(\theta) = \mathbf{0}, \mathbf{F}_b + \mathbf{F}_g = \mathbf{0}, \mathbf{F}_{th} + \mathbf{F}_d = \mathbf{0}, \quad (2)$$

where r_t^b is the distance between c_b and c_t , r_z^b is the distance between c_b and c_g , and m_{rb} is the MBR total mass.

B. Inverted Control Problem Statement

According to Equations (1) and (2), the MBR is a highly nonlinear system, driven by horizontal and vertical thrusters. Its attitude control is susceptible to variations in the dynamic model parameters. This paper aims to design a robust control policy π_α that drives the MBR from the stable equilibrium (Θ_0) to reach and stabilize around the unstable equilibrium point (Θ_d). The orientation of the MBR is denoted by the $\Theta = [\phi, \theta, \psi]^T$. The control objective can be expressed as:

$$\lim_{t \rightarrow \infty} \|\Theta_d - \Theta_t\|_{M_\Theta} = 0, \Theta_t = T_b(\Theta_{t-1}, \mathbf{a}_t, \mathbf{S}_b), \quad (3)$$

where T_b is the dynamics transition from Θ_{t-1} to Θ_t under the control command \mathbf{a}_t that is generated by the designed policy π_α . \mathbf{S}_b involves the parameters in the MBRs' dynamic model.

The policy π_α aims to maximize the total cumulative reward the MBR receives over the long run through interaction with the environment, formulated as:

$$\max_{\alpha} G_t \quad (4)$$

$$\text{s.t. } G_t = \sum_{k=0}^{\infty} \gamma^k r_{t+k+1}, r_t = f_r(\mathbf{s}_t, \mathbf{s}_{t+1}, \mathbf{a}_t), \quad (5)$$

$$\mathbf{s}_{t+1} = T_b^v(\mathbf{s}_t, \mathbf{a}_t, \mathbf{S}_b^v), \mathbf{a}_t = \pi_\alpha(\mathbf{s}_t), \quad (6)$$

where G_t is the cumulative reward. γ is the discount factor, and f_r is the designed reward function to evaluate the action \mathbf{a}_t taken in state \mathbf{s}_t . T_b^v and \mathbf{S}_b^v represent the dynamics transition and the parameters of the MBR in the simulation environment, respectively.

Due to unmodeled dynamics and parameter mismatches in the training environment, bridging the gap between the simulated environment and the physical setting needs to

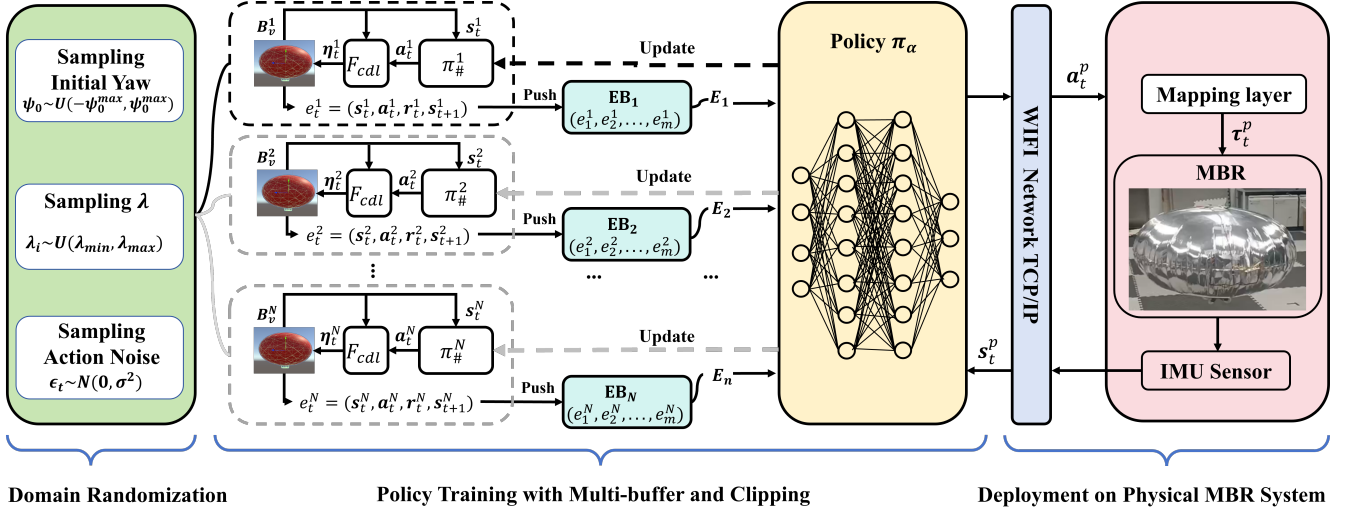


Fig. 3: Pipeline of developing and deploying robust policy for inverted control of MBRs.

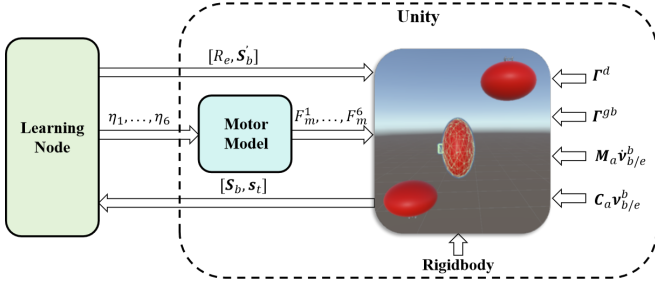


Fig. 4: 3D simulation environment designed for robust policy learning for inverted control of MBRs.

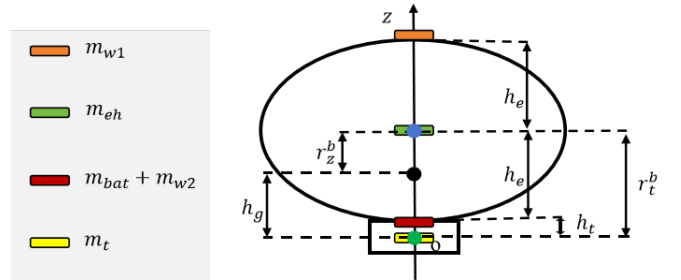


Fig. 5: The MBR's structure in the simulation environment.

be considered in the policy deployment phase. Assuming there is a mapping function f_m that can bridge the gap, the problem is formulated as:

$$\lim_{t \rightarrow \infty} \|s_d - s_t\|_{M_s} = 0, \quad (7)$$

$$s_{t+1} = T_b^p(s_{t-1}, \mathbf{a}_t^p, \mathbf{S}_b^p), \mathbf{a}_t^p = f_m(\pi_\alpha(s_t)), \quad (8)$$

where $T_b^p \neq T_b^v$ and $\mathbf{S}_b^v \neq \mathbf{S}_b^p$. s_d is the desired state.

III. METHODOLOGY

The pipeline of learning a robust policy for inverted control of MBRs is illustrated in Fig. 3, which incorporates three core stages: (1) 3D simulation environment creation, (2) Physics-informed domain randomization strategy design, and (3) TD3 with multi-buffer and clipping.

A. Simulation Environment

As illustrated in Fig. 4, Unity was selected as the platform to implement MBR's dynamics and construct the policy training settings. The Rigidbody component was utilized to replicate Equation (1), with several self-implementation forces using two APIs: AddForceAtPosition and AddRelativeTorque, including the air drag Γ^d , the restoring force and torque Γ^{gb} , and the terms (M_a and C_a) resulting from added mass and added inertial tensor. Parameter identification was

conducted using the methods in [22], [23]. To optimize the simulator for inverted control policy training, three enhancements were implemented. Firstly, based on collected physical data, a more precise motor model was developed and calibrated by using the model identification method [24], expressed as:

$$F_m = g_m(-0.0292\eta^2 + 0.1118\eta - 0.0039), \quad (9)$$

where g_m is the motor's gain parameter. Adjusting g_m allows the simulation of a variety of motor models. F_m represents the thrust generated by the motor under the command $\eta \in [0, 1]$. Secondly, the simulated MBR's structure was enhanced, as shown in Fig. 5. This modification splits the total extra weight into two components (m_{w_1} and m_{w_2}) to facilitate inverted control policy training. Thirdly, a new learning node, implemented as a Python script, provides the capability to restart a new episode by issuing an environment reset command R_e , and to configure MBR parameters \mathbf{S}_b' online. The terms \mathbf{S}_b and s_t are the real-time MBR's parameters and state, respectively. The learning node obtains the dynamics transition $(s_t, \mathbf{a}_t, s_{t+1})$ by sending motor commands and receiving the real-time state.

B. Physics-informed Domain Randomization

As analyzed in Section II-A, the distances between the three center points (c_b , c_g and c_t) play a dominant role in the

dynamics of the MBR. Our domain randomization strategy focuses on modifying these distances while maintaining physical consistency. As shown in Fig. 5, the total average mass and the point of gravity application are located at c_g . The distance between c_g and c_t is

$$h_g = \frac{(m_{bat} + m_{w2})h_t + (m_e + m_h)r_t^b + m_{w1}(2h_e + h_t)}{m_{rb}}, \quad (10)$$

where the total mass $m_{rb} = m_t + m_{bat} + m_e + m_h + m_{w1} + m_{w2}$. m_t and m_{bat} are the weights of the gondola and the battery, respectively. $m_w = m_{w1} + m_{w2}$ is the extra weight to ensure that the MBR is in the neutrally buoyant state. m_e is the weight of the envelope in the deflated state, while m_h is the weight of the filled helium, calculated by $m_h = \rho_h V$, where ρ_h is the density of helium and V is the total volume of the inflated envelope. The distance between c_g and c_b is $r_z^b = r_t^b - h_g$, where $r_t^b = h_t + h_e$. h_t and h_e are half-heights of the gondola and the inflated envelope, respectively. Denote $m_{w1} = \lambda m_w$ and $m_{w2} = (1 - \lambda)m_w$, h_g can be expressed in a simple way, as

$$h_g = \frac{d_m + m_w(h_t + 2\lambda h_e)}{m}, \quad (11)$$

where $d_m = m_{bat}h_t + (m_e + m_h)r_z^b$. Adjusting m_w and λ can modify the distances between these center points. The key distinction is that only varying λ allows m_w to remain constant while altering h_g .

C. TD3 with Multi-buffer and Clipping

TD3 [25], one of the off-policy DRL algorithms, involves two synchronized subprocesses: environmental interaction and policy improvement. The goal of environmental interaction is to sample the MBR's trajectories in response to various actions, where the feedback from each action is quantified by its corresponding reward. As outlined in Algorithm 1, N replay buffers, the output of the algorithm, are employed to store trajectories of the MBR with different λ .

Once the experience buffers are populated, a separate thread is utilized to enhance the policy, as detailed in Algorithm 2. The main algorithm structure adheres to the TD3 method and incorporates a gradient clipping operation (c_α and c_β) adopted from the PPO method [26], to further enhance training stability. Rather than training the policy on a single experience buffer, it is updated using N distinct experience buffers, each containing data from different MBR dynamics. In this way, the policy is trained to capture more general features, enabling it to perform successfully across a wide range of scenarios.

The MBR's state comprises the rotation matrix \mathbf{R} and angular velocities ω . The action consists of the desired torques about the three rotational axes, which are subsequently converted into motor commands using the functional module F_{cdl} mentioned in Fig. 3. Its implementation followed the approach outlined in [24].

The reward function comprises three components: an orientation reward r_{rot} , an angular velocity cost r_ω , and an

Algorithm 1: Environmental Interaction with Domain Randomization

Data: Behavior policies $\pi_\#$, N replay buffers $\mathcal{B}_1, \dots, \mathcal{B}_N$, running time of each episode t_e , maximum episode N_e , gaussian noise parameters σ , ξ and n_σ , N variable parameters $\lambda_1, \dots, \lambda_N$, $k = 0$

Result: N replay buffers with experiences

```

for  $i = 1$  to  $N_e$  do
  if  $i \bmod n_\sigma = 0$  then
     $\sigma \leftarrow \xi \sigma$ 
     $t_s \leftarrow \text{GetCurrentSystemTime}$ 
     $\psi^i \leftarrow U(-\psi_0, \psi_0)$ 
     $\text{UpdateBlimpParameter}(\lambda_k, \psi^i)$ 
  while True do
     $\epsilon_t^k \sim \mathcal{N}(0, \sigma^2)$ 
    Observe state  $s_t^k$ , select action
     $a_t^k = \pi_\#(s_t^k) + \epsilon_t^k$ 
     $\phi_t^k, \theta_t^k \leftarrow \text{GetAttitudeAngles}(s_t^k)$ 
     $\eta_t^k \leftarrow F_{cdl}(a_t^k, \phi_t^k, \theta_t^k)$ 
    Execute  $\eta_t^k$ , observe reward  $r_t^k$ , next state
     $s_{t+1}^k$ , done flag  $d_t^k$ 
    Store  $(s_t^k, a_t^k, r_t^k, s_{t+1}^k, d_t^k)$  in  $\mathcal{B}_k$ 
     $k \leftarrow k + 1$ 
  if  $k == N$  then
     $k = 0$ 
     $t_c \leftarrow \text{GetCurrentSystemTime}$ 
    if  $t_c - t_s \leq t_e$  or over range then
      break

```

action cost r_a , which can be expressed as

$$r_{total} = r_{rot} + r_\omega + r_a, \quad (12)$$

where $r_\omega = -\frac{\sum_{i \in \{x, y, z\}} g_{\omega_i} |\omega_i|}{\omega_{max}}$. The parameter g_{ω_i} represents the weight assigned to each channel, and ω_{max} denotes the maximal angular velocity. The action cost is denoted by $r_a = -\sum_{i \in \{x, y, z\}} g_{ai} |\tau_i|$, where g_{ai} is the parameter to shape the reward, and τ_i represents the expected torque of the i -th axis. The orientation reward is defined as

$$r_{rot} = \exp(-\text{clip}(g_\phi |e_\phi| + g_\theta |e_\theta| + g_\psi |e_\psi|, 0, g_n)) + \mathbb{I}_{\{\varphi < \zeta\}} \cdot \left(1 - \frac{\varphi}{\zeta}\right), \quad (13)$$

where $e_\phi = \frac{\varphi \mathbf{v}_x}{\pi}$, $e_\theta = \frac{\varphi \mathbf{v}_y}{\pi}$ and $e_\psi = \frac{\varphi \mathbf{v}_z}{\pi}$. The pair (\mathbf{v}, φ) represents the axis-angle parameterization of the orientation error $\mathbf{R}_e = \mathbf{R}^T \mathbf{R}_d$, where $\mathbf{R}_d = \text{diag}(1, -1, -1)$. The rotation angle φ is calculated by $\varphi = \arccos(\min(\max(\frac{\text{tr}(\mathbf{R}_e) - 1}{2}, -1), 1))$, and the rotation axis is

given by: $\mathbf{v} = \frac{1}{2 \sin \varphi} \begin{bmatrix} \mathbf{R}_{e32} - \mathbf{R}_{e23} \\ \mathbf{R}_{e13} - \mathbf{R}_{e31} \\ \mathbf{R}_{e21} - \mathbf{R}_{e12} \end{bmatrix}$. The symbol \mathbb{I} denotes

the indicator function where the value is equal to 1 if the condition is true, 0 otherwise. The parameter ζ represents the threshold for the precision bonus.

Algorithm 2: TD3 with Multi-Buffer and Clipping

Data: N replay buffers $\mathcal{B}_1, \dots, \mathcal{B}_N$, interval of policy delay update d_p , discount γ , target network update rate ϖ , thresholds for gradient clipping c_α and c_β , actor π_α , critics Q_{β_1}, Q_{β_2} , target networks $\pi_{\alpha'}, Q_{\beta'_1}, Q_{\beta'_2}$

Result: Learned policy π_α

while *True* **do**

for *buffer* $k = 1$ **to** N **do**

 Sample batch $(s_i^k, a_i^k, r_i^k, s_{i+1}^k, d_i^k) \sim \mathcal{B}_k$

Critics Update: Aggregate target Q-values: $Q_d =$

$$\frac{1}{N} \sum_{k=1}^N \left[r_i^k + \gamma(1 - d_i^k) \min_{j=1,2} Q_{\beta'_j}(s_{i+1}^k, \pi_{\alpha'}(s_{i+1}^k)) \right]$$

 Update gradients ($j = 1, 2$):

$$\nabla_{\beta_j} = \frac{1}{N} \sum_{k=1}^N \sum_i (Q_{\beta_j}(s_i^k, a_i^k) - Q_d)^2$$

 Clip gradients: $\text{clip}(\nabla_{\beta_j}, -c_\beta, c_\beta)$

Delayed Actor Update:

if $t \bmod d_p = 0$ **then**

 Update gradients π_α :

$$\nabla_\alpha = \frac{1}{N} \sum_{k=1}^N \sum_i Q_{\beta_1}(s_i^k, \pi_\alpha(s_i^k))$$

 Clip gradients: $\text{clip}(\nabla_\alpha, -c_\alpha, c_\alpha)$

Target Network Updates:

 Soft update: $\beta'_j \leftarrow \varpi \beta_j + (1 - \varpi) \beta'_j$ for $j = 1, 2$

 Soft update: $\alpha' \leftarrow \varpi \alpha + (1 - \varpi) \alpha'$

TABLE I: Parameters in the reward function

$g\omega_x$	$g\omega_y$	$g\omega_z$	$g a_x$	$g a_y$	$g a_z$	$g\phi$	$g\theta$	$g\psi$	ζ	g_n
0.01	0.01	0.01	0.001	0.001	0.001	5.0	5.0	0.5	0.1	10

D. Implementation Details

A fully connected network architecture with two hidden layers was employed to approximate both the policy π_α and the action-value function Q_β . Each hidden layer consists of 256 neurons. Except for the policy’s output layer, which uses a hyperbolic tangent (Tanh) activation function, all other layers employ the leaky rectified linear unit (Leaky ReLU). The network architecture and parameter updates were implemented using the PyTorch library. The parameters and their corresponding values in the reward function are listed in Table I. Notably, the deviations in roll and pitch angles are assigned higher weights than that of the yaw angle. The desired MBR behavior is to rapidly reach and maintain an inverted pose, followed by adjusting the yaw angle to zero. At the same time, energy consumption must be minimized, as the reward function includes a penalty for action.

The parameters and their corresponding values used in Algorithms 1 and 2 are provided in Table II. Ten buffers were used to store experiences sampled across different values of λ , which were constrained to the interval $[0.6, 1.0]$, given the MBR parameters outlined in [24]. The motor gain g_m was set to 1.7 during the policy training process.

TABLE II: Parameters in policy training

N	t_e	N_e	σ	ξ	n_σ	d_p	γ	ϖ	c_a	c_b	λ	ψ_0
10	30s	500	0.15	0.95	100	2	0.98	0.01	0.1	0.1	[0.6, 1]	0.5

TABLE III: Comparison of the baseline controller and the trained policy with varied m_w

Method	$m_w = 5g$	$m_w = 10g$	$m_w = 15g$	$m_w = 20g$	$m_w = 25g$
Baseline	×	×	×	×	✓
Our policy	×	✓	✓	✓	✓

IV. EVALUATION AND EXPERIMENT

To evaluate the effectiveness and robustness of the trained policy, the parameters m_w , λ , and g_m were varied individually in the task of achieving and maintaining the inverted pose. The energy-shaping controller presented in [17] was used as the baseline for comparison. The coefficients for this controller were tuned under the specific conditions of $m_w = 23.35$ g, $\lambda = 1$, and $g_m = 1.7$.

A. Performance of the Trained Policy to m_w Variations

As shown in Table III, the results were obtained by altering only the total extra weight m_w , while keeping $\lambda = 1$ and $g_m = 1.7$ constant. The value of m_w was adjusted from 5 g to 25 g, causing the magnitude of buoyancy to vary from being greater than gravity to less than gravity. When $m_w = 5$ g, neither the trained policy nor the controller can finish the mission. This is because c_g is too close to c_t , making it impossible to invert the MBR under the given motor gain $g_m = 1.7$. In all other cases, the trained control policy accomplishes the task, whereas the baseline controller only functions at $m_w = 25$ g. This demonstrates that a controller dependent on specific system energy relationships fails when the blimp’s parameters change.

The intended outcome of the mission is to transition the roll angle from 0 to π while maintaining both the pitch and yaw angles at 0. The variations in the roll angle across these cases are illustrated in Fig. 6. The terms m_w^π and m_w^c correspond to the trained control policy and the baseline controller, respectively. As m_w increases, the maximal achievable roll angle rises until it reaches $\phi = \pi$. The neutrally buoyant weight is approximately 23.35 g. Therefore, when $m_w = 25$ g, the magnitude of buoyancy is less than that of gravity. As a result, the maximum achievable roll angle is larger than in other cases because c_g is closer to c_b .

B. Performance of the Trained Policy to λ Variations

Varying λ determines the position of c_g while maintaining the MBR in a neutrally buoyant state. In this experiment, the extra weight and motor gain were set to $m_w = 23.35$ g and $g_m = 1.7$, respectively. Table IV presents the results for both the baseline controller and the trained control policy, indicating that the baseline controller was only successful when $\lambda = 1.0$.

The trained control policy completes the task for all $\lambda \in [0.6, 1.0]$, demonstrating its robustness against variations in

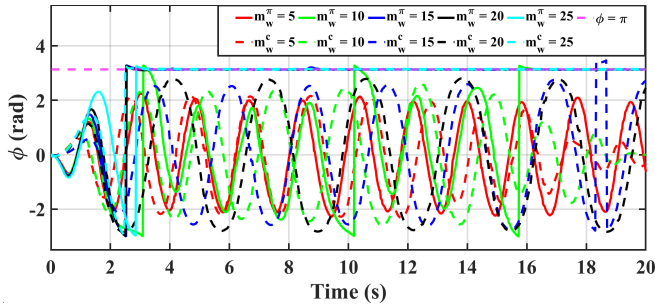


Fig. 6: Roll angle variations with changes in m_w .

TABLE IV: Comparison of the baseline controller and the trained policy with varied λ

Method	$\lambda = 0.6$	$\lambda = 0.7$	$\lambda = 0.8$	$\lambda = 0.9$	$\lambda = 1.0$
Baseline	×	×	×	×	✓
Our policy	✓	✓	✓	✓	✓

MBR parameters. The variations in the roll angle under these conditions are depicted in Fig. 7, in which the parameter for the policy is denoted as λ^π and that for the controller as λ^c . Unlike the variation in m_w , changes in λ do not affect the magnitudes of buoyancy and gravity, but only influence the position of c_g . As λ increases, c_g moves closer to c_b . This results in larger maximum achievable roll angles (before reaching $\phi = \pi$) and reduces the time required to achieve the inverted state. When $\lambda = 1.0$, the controller completed the task more quickly, as its parameters were specifically fine-tuned for this configuration.

C. Performance of the Trained Policy to g_m Variations

To verify that the trained policy functions effectively across different motors, m_w and λ are configured to 23.35 g and 1.0, respectively. The results are shown in Table V.

TABLE V: Comparison of the baseline controller and the trained policy with varied g_m

Method	$g_m = 0.5$	$g_m = 1.0$	$g_m = 1.5$	$g_m = 2.0$	$g_m = 2.5$
Baseline	×	✓	✓	✓	✓
Our policy	×	✓	✓	✓	✓

Only in the case where $g_m = 0.5$ did both the policy and the controller fail. Although they were able to generate control laws that brought the MBR to an inverted pose, the motors generated insufficient forces to maintain this state. At approximately 9 seconds, the MBR, under controller adjustment, reached the inverted pose. Around 11 seconds, the policy successfully inverted the MBR. Although both the controller and the policy are capable of completing the mission, their control effects differ, as illustrated in Fig. 8. The results indicate that as g_m increases, less time is required for the policy to complete the task due to the corresponding increase in total force. When $g_m \geq 2.0$, only two rotations are necessary, a result consistent with the controller method. In contrast, for the controller, a higher g_m results in a larger

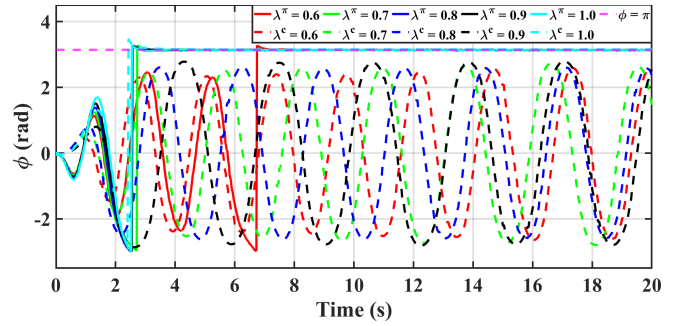


Fig. 7: Roll angle variations with changes in λ .

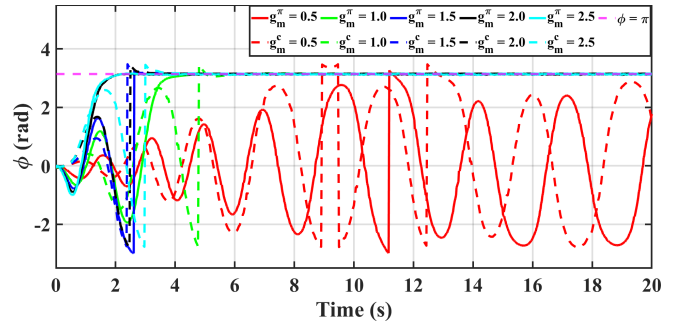


Fig. 8: Roll angle variations with changes in g_m .

maximum achievable roll angle, which in turn requires more time to complete the task.

D. Performance of the Trained Policy to m_w , λ and g_m Variations

The parameters m_w , λ , and g_m were varied simultaneously to further validate the trained policy. The specific configurations and results are detailed in Table VI. The trained policy succeeded in all cases, while the controller failed. The variations in the roll angle are illustrated in Fig. 9. In case 2 (C2), the MBR required more time to complete the maneuver due to the low value of g_m .

TABLE VI: Comparison of the baseline controller and the trained policy with varied m_w , λ , and g_m

Test Case	C1	C2	C3	C4	C5
m_w (g)	15	15	20	25	25
λ	0.8	1.0	0.9	0.7	0.8
g_m	1.7	1.0	1.6	1.5	1.4
Baseline	×	×	×	×	×
Our Policy	✓	✓	✓	✓	✓

E. Ablation Study

To demonstrate the effectiveness of the multi-buffer approach and gradient clipping in stabilizing the training process, an ablation study was conducted. The results are presented in Fig. 10. The proposed method, which incorporates both multi-buffer experience storage and gradient clipping, converged to an effective policy in approximately 100 episodes. In contrast, the version using multi-buffer

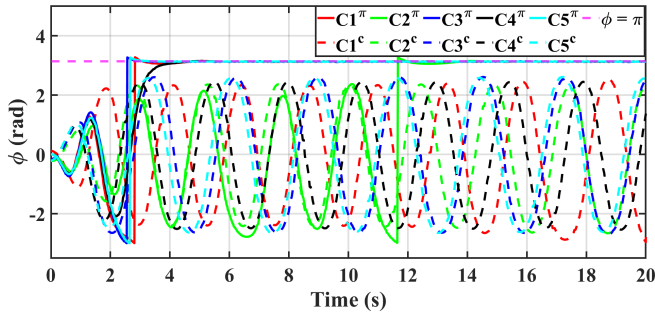


Fig. 9: Roll angle variations with changes in m_w , λ and g_m .

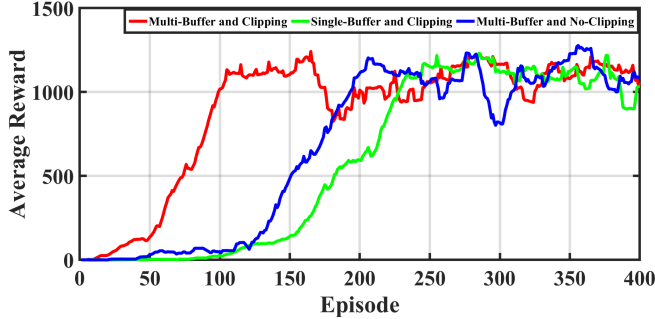


Fig. 10: Comparison of the average reward across three cases, computed using a moving average with a window size of 19.

storage without clipping required nearly 200 episodes to achieve a similar policy. Furthermore, the approach utilizing a single buffer with gradient clipping required a minimum of 250 episodes to train the policy, making it 2.5 times slower than the proposed method. In the experiment, the capacity of the single buffer was set equal to the combined capacity of all buffers in the multi-buffer setup. This confirms that the multi-buffer strategy, combined with gradient clipping, stabilizes the training process and enables the method to reliably converge to a policy using significantly fewer episodes of experience collection. Due to the persistent inclusion of action noise ϵ_t^k during the entire training process, the average return exhibits continuous fluctuations.

F. Policy Deployment in Physical MBRs

Inspired by the traditional control design pipeline, where controller parameters are manually tuned for each physical system, we try to transfer the trained policy to the physical system with only minimal parameter adjustments, eliminating the need for further training using physical data. As shown in Fig. 3, a mapping layer was introduced to bridge the sim-to-real gap during the process of achieving the inverted pose, as

$$\tau^p = \mathbf{M}_0 \mathbf{a}^p, \Delta_\phi < \varrho, \quad (14)$$

where $\tau^p = [\tau_x, \tau_y, \tau_z]^T$. $\Delta_\phi = \pi - \phi$ is the deviation between the target and current roll angles, and ϱ is the threshold for switching. In the experiment, $M_0 = \text{diag}(m_\phi, m_\theta, m_\psi)$, and ϱ is equal to 0.8. Keeping $m_\theta = 0.1$ and $m_\psi = 0.1$, m_ϕ varies from 0.5 to 0.8. The results under different m_ϕ are shown in Fig. 11, where the trained policy was used

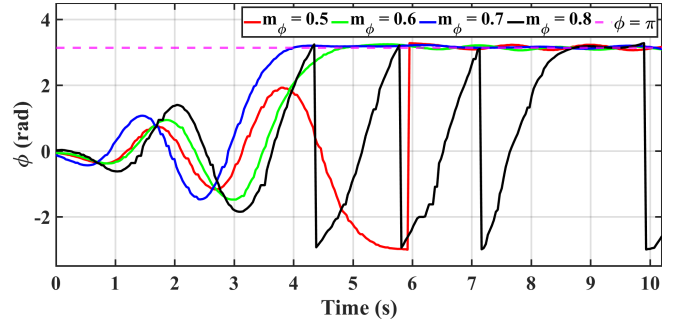


Fig. 11: Roll angle variations of the MBR with different m_ϕ .

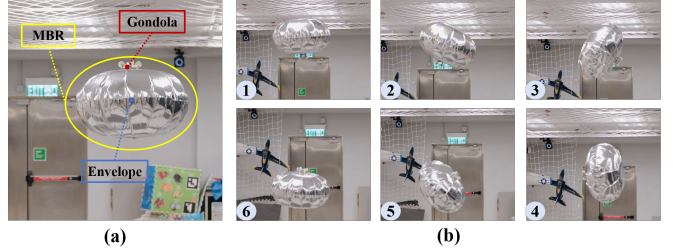


Fig. 12: (a) Experimental setup; (b) Visualization of the action sequence of an MBR for achieving an inverted pose.

to achieve the inverted pose while a PD controller was utilized to maintain the state. The action sequence of an MBR achieving the inverted pose is illustrated in Fig. 12 for the case where $m_\phi = 0.7$. When the angular velocities of the MBR are close to zero, the PD controller stabilizes the MBR in the inverted pose. Different m_ϕ can let the trained policy have various behaviors in the physical system. In these tests, only $m_\phi = 0.8$ cannot achieve the mission. The experimental results demonstrate that it is possible to bridge the sim2real gap without further policy training by designing a mapping layer. Using the coefficient $m_\phi = 0.7$, the performance of the trained policy was further validated on the physical MBR by adjusting m_{w1} and m_{w2} to create five test cases, as detailed in Table VII. In all cases, the MBR succeeded in reaching the inverted pose, as shown in Fig. 13. Increasing m_{w1} brings c_g close to c_b , thereby reducing the time required to achieve the inverted pose. Conversely, adding m_{w2} moves c_g close to c_t , which increases the time needed to finish the mission. The results of the training policy in the physical system are consistent with those presented in Sections IV-A and IV-B.

TABLE VII: Configuration of the extra weights in the physical experiment

Weights	MBR_1	MBR_2	MBR_3	MBR_4	MBR_5
$m_{w1}(g)$	25	26.07	25	27.59	25
$m_{w2}(g)$	0	0	1.07	0	2.59

V. CONCLUSION

This paper proposes a new DRL-based method for inverted control of MBR, aiming to achieve its full agility.

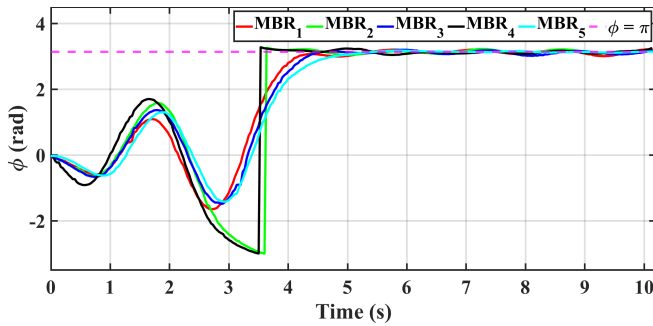


Fig. 13: Roll angle variation of the MBR with different m_w .

The method involves the construction of a virtual training environment, policy training using domain randomization and an improved TD3 method, and policy deployment via a designed mapping layer. Compared to the energy-shaping controller, the learned policy achieves a higher success rate across diverse scenarios. Although the mapping layer designed for policy deployment enables the policy to function in physical settings without further training, it constrains the performance of the trained policy. This indicates that a linear relationship alone cannot fully bridge the sim-to-real gap. Therefore, analyzing and quantifying the sim-to-real gap in inverted control remains an open problem for future work.

REFERENCES

- [1] M. Wang, Q. Wang, Z. Wang, Y. Gao, J. Wang, C. Cui, Y. Li, Z. Ding, K. Wang, C. Xu, *et al.*, “Unlocking aerobatic potential of quadcopters: Autonomous freestyle flight generation and execution,” *Science Robotics*, vol. 10, no. 101, p. eadp9905, 2025.
- [2] G. Torrente, E. Kaufmann, P. Föhn, and D. Scaramuzza, “Data-driven mpc for quadrotors,” *IEEE Robotics and Automation Letters*, vol. 6, no. 2, pp. 3769–3776, 2021.
- [3] Y. Xie, M. Lu, R. Peng, and P. Lu, “Learning agile flights through narrow gaps with varying angles using onboard sensing,” *IEEE Robotics and Automation Letters*, vol. 8, no. 9, pp. 5424–5431, 2023.
- [4] Z. Han, X. Huang, Z. Xu, J. Zhang, Y. Wu, M. Wang, T. Wu, and F. Gao, “Reactive aerobatic flight via reinforcement learning,” *arXiv preprint arXiv:2505.24396*, 2025.
- [5] S. Oh, S. Kang, K. Lee, S. Ahn, and E. Kim, “Flying display: Autonomous blimp with real-time visual tracking and image projection,” in *2006 IEEE/RSJ International Conference on Intelligent Robots and Systems*. IEEE, 2006, pp. 131–136.
- [6] H. Han and B. D. Song, “The flying warehouse delivery system with multi-commodity inventory management,” *Available at SSRN 4988309*, 2024.
- [7] D. Chaitanya, M. N. Reddy, V. M. Shaju, P. J. Bharadwaz, B. S. Jayanth, and M. Bukya, “Slam-enabled autonomous blimp for uav applications,” in *2025 International Conference on Next Generation Communication & Information Processing (INCIP)*. IEEE, 2025, pp. 1034–1039.
- [8] Y. Nitta, S. Inai, K. Matsumura, M. Ishida, T. Onai, and A. Nishitani, “The visual inspection methodology for ceiling utilizing the blimp,” *Procedia Engineering*, vol. 188, pp. 256–262, 2017.
- [9] Y. Zhang, J. Yan, X. Fan, S. Wang, X. Wang, W. Huang, and Z. Zhao, “A novel miniature omnidirectional multi-rotor blimp,” in *2023 IEEE 18th Conference on Industrial Electronics and Applications (ICIEA)*. IEEE, 2023, pp. 1568–1573.
- [10] S. Ye, J. Zhang, Q. Lu, Y. Xiao, J. Yuan, and S. Hu, “Design and simulation of a bio-inspired rigid-soft hybrid robotic blimp,” in *2022 International Conference on Advanced Robotics and Mechatronics (ICARM)*. IEEE, 2022, pp. 599–604.
- [11] J. Xu, D. S. D’antonio, D. J. Ammirato, and D. Saldaña, “Sblimp: Design, model, and translational motion control for a swing-blimp,” in *2023 IEEE/RSJ International Conference on Intelligent Robots and Systems (IROS)*. IEEE, 2023, pp. 6977–6982.
- [12] Q. Tao, J. Wang, Z. Xu, T. X. Lin, Y. Yuan, and F. Zhang, “Swing-reducing flight control system for an underactuated indoor miniature autonomous blimp,” *IEEE/ASME Transactions on Mechatronics*, vol. 26, no. 4, pp. 1895–1904, 2021.
- [13] S. Cho, V. Mishra, Q. Tao, P. Vamell, M. King-Smith, A. Muni, W. Smallwood, and F. Zhang, “Autopilot design for a class of miniature autonomous blimps,” in *2017 IEEE conference on control technology and applications (CCTA)*. IEEE, 2017, pp. 841–846.
- [14] H. Cheng, Z. Sha, Y. Zhu, and F. Zhang, “Rgblimp: robotic gliding blimp-design, modeling, development, and aerodynamics analysis,” *IEEE Robotics and Automation Letters*, vol. 8, no. 11, pp. 7273–7280, 2023.
- [15] J. Xu, T. Vu, D. S. D’Antonio, and D. Saldaña, “Mochiswarm: A testbed for robotic blimps in realistic environments,” *arXiv preprint arXiv:2503.03077*, 2025.
- [16] M. Pellegrino, M. Barciś, J. Simonjan, Zulkarnaen, C. F. Chiasserini, and E. Natalizio, “Tinyblimp: A promising frontier for autonomous miniature unmanned aerial vehicles,” in *Proceedings of the 10th Workshop on Micro Aerial Vehicle Networks, Systems, and Applications*, 2024, pp. 1–6.
- [17] J. Wang and F. Zhang, “Achieving and maintaining inverted pose for miniature autonomous blimps,” in *2024 American Control Conference (ACC)*. IEEE, 2024, pp. 338–343.
- [18] Y. T. Liu, E. Price, M. J. Black, and A. Ahmad, “Deep residual reinforcement learning based autonomous blimp control,” in *2022 IEEE/RSJ International Conference on Intelligent Robots and Systems (IROS)*. IEEE, 2022, pp. 12566–12573.
- [19] Y. Zuo, Y. T. Liu, and A. Ahmad, “Autonomous blimp control via h_∞ robust deep residual reinforcement learning,” in *2023 IEEE 19th International Conference on Automation Science and Engineering (CASE)*. IEEE, 2023, pp. 1–8.
- [20] Unity Technologies, “Unity: Real-time development platform — 3d, 2d, vr & ar engine.” [Online]. Available: <https://unity.com>
- [21] J. Dong, H. Yu, B. Lu, H. Liu, and Y. Fang, “Adaptive output feedback trajectory tracking control of an indoor blimp: Controller design and experiment validation,” *IEEE Transactions on Industrial Electronics*, 2024.
- [22] Q. Tao, J. Cha, M. Hou, and F. Zhang, “Parameter identification of blimp dynamics through swinging motion,” in *2018 15th International Conference on Control, Automation, Robotics and Vision (ICARCV)*. IEEE, 2018, pp. 1186–1191.
- [23] Q. Tao, M. Hou, and F. Zhang, “Modeling and identification of coupled translational and rotational motion of underactuated indoor miniature autonomous blimps,” in *2020 16th international conference on control, automation, robotics and vision (ICARCV)*. IEEE, 2020, pp. 339–344.
- [24] Q. Tao, “Design and control of an indoor miniature autonomous blimp,” *Ph. D. dissertation, Georgia Institute of Technology*, 2020.
- [25] S. Fujimoto, H. Hoof, and D. Meger, “Addressing function approximation error in actor-critic methods,” in *International conference on machine learning*. PMLR, 2018, pp. 1587–1596.
- [26] J. Schulman, F. Wolski, P. Dhariwal, A. Radford, and O. Klimov, “Proximal policy optimization algorithms,” *arXiv preprint arXiv:1707.06347*, 2017.